Supplementary Information: Persistent fluid flows defined by active matter boundaries

Zijie Qu[1], Dominik Schildknecht[1], Shahriar Shadkhoo[1], Enrique Amaya[1], Jialong Jiang[1], Heun Jin Lee[2], David Larios[1], Fan Yang[1], Rob Phillips[1,2,3], and Matt Thomson[1]

[1]Division of Biology and Biological Engineering, California Institute of Technology, Pasadena, California, 91125, USA.
[2]Department of Applied Physics, California Institute of Technology, Pasadena, California, 91125, USA.
[3]Department of Physics, California Institute of Technology, Pasadena, California, 91125, USA.

August 19, 2021

Supplementary Methods 1: Flow cell

The flow cell is made by sandwiching a paraffin film (Parafilm M) between a glass slide and a coverslip, both are treated with a hydrophilic acrylamide coating [1, 2]. The paraffin film is heated at 65 °C on top of the glass slide for 10 s, then the coverslip is put above the paraffin film and gently pressed for 15 s until properly sealed. The final size of the flow cell is 50 mm in length, 3 mm in width and approximately 70 µm in depth.

Supplementary Methods 2: Illumination Protocol

In this work, we follow the same illumination protocol as in [2] where we activate motor-linking with pulsed light. Specifically, we project a given light pattern onto the active matter system every 10 s, and the duration of each light pulse is 30 ms. There are two reasons we use the pulsed illumination protocol. First, the motors that are activated during the 30 ms illumination interval are sufficient to generate network contraction and sustained fluid flow. With less illumination, we do not observe sufficient cross-linked microtubules for network formation, and therefore, do not observe fluid flow. Second, if we choose longer illumination (either higher pulsing frequency or even a continuous illumination), we observe activated motor outside of the illumination region which can cause a cross-linked network to form outside the illumination region. The activated motor has a "lifetime" (30 s half-life). With increased illumination frequency, we increase the probability that still activated motor leaves the illumination region (as a result of the fluid flow). Activated motors that escape the illumination region due to transport will cause microtubule network formation and contraction outside the illumination region. In practice, such motor transport can lead to changes in the microtubule network architecture that disturb the steady-state fluid flow. In theory, one could lower the illumination (light intensity) and constantly project the light pattern to achieve the same fluid flow result. However, since we do not yet fully understand the relationship between the number of activated motors vs light intensity, we choose to apply a constant and well controlled periodic illumination as in [2].

Supplementary Methods 3: Measuring the flow field with particle tracking velocimetry (PTV)

The flow field is measured by tracking individual particle from frame to frame [3]. The inert particles are visualized using bright-field microscopy. The images are pre-processed with a Gaussian filter in Matlab (MathWorks) with standard deviation of 1 intensity unit to reduce the noise level, then with a binary filter to distinguish the detected particles from the backgrounds. The centroid of each particle is measured by the regionprops function in Matlab. The particle pairs between subsequent images are determined with a nearest-neighbor algorithm [4] with a 8.8 µm distance threshold. The resultant distance vectors are then grouped and averaged within a 17.6 µm square as the mesh grid for the flow field. Finally, the vector fields are averaged temporally over the entire experimental process.

Supplementary Methods 4: Particle image velocimetry (PIV) analysis of microtubule flow field

The particle image velocimetry is performed by a custom code written in Matlab [5]. After intensity adjustment of the images, the microtubule velocity field is determined by using the "imregdemons" built-in function of Matlab, which measures the displacement field between images at two successive time points. This function is based on the diffeomorphic demons algorithm incorporated into the diffusing model of pattern matching, and uses an efficient second-order minimization method. The optimal transformation, between the fixed and transformed images, minimizes the differences between the pixel values as well as the gradients.

To validate our PIV method, we applied our PIV analysis procedure as well as PIVLab to simulated images of a contracting microtubule network (Supplementary Figure 1). We generate synthetic data for linked microtubules, and we used this data to generate synthetic images which were, then, applied as inputs to PIVlab and our PIV analysis based on Matlab . We found that our Matlab PIV analysis code infers a velocity field that has a correlation coefficient with simulated data of mean $\mu_C = 0.816$ and standard deviation $\sigma_C = 0.062$ (calculated as mean and standard deviation across the time-series) with the simulated data while PIVLab had a correlation coefficient of $\mu_C = 0.155$ and $\sigma_C = 0.1617$

Supplementary Note 1: Microtubule filament transportation measurement

Microtubule filaments are transported by the fluid flow through the experiments and we measure this phenomenon by referring to the change in intensity within the illumination region. In Supplementary Figure 2, we plot the intensity within the illumination region of the 600 µm square experiment. The intensity is a summation of all pixel values within the illumination region and normalized by the one measured at the first frame of the experiment. It is observed that the intensity is increasing over time, indicating the accumulation of microtubule filaments.

Supplementary Methods 5: Image Segmentation, microtubule network size analysis

Traditional computer vision techniques available in Python 3.7 [6, 7] were applied to segment microtubule-network regions in every frame of the movie. In the preprocessing steps, we rescaled

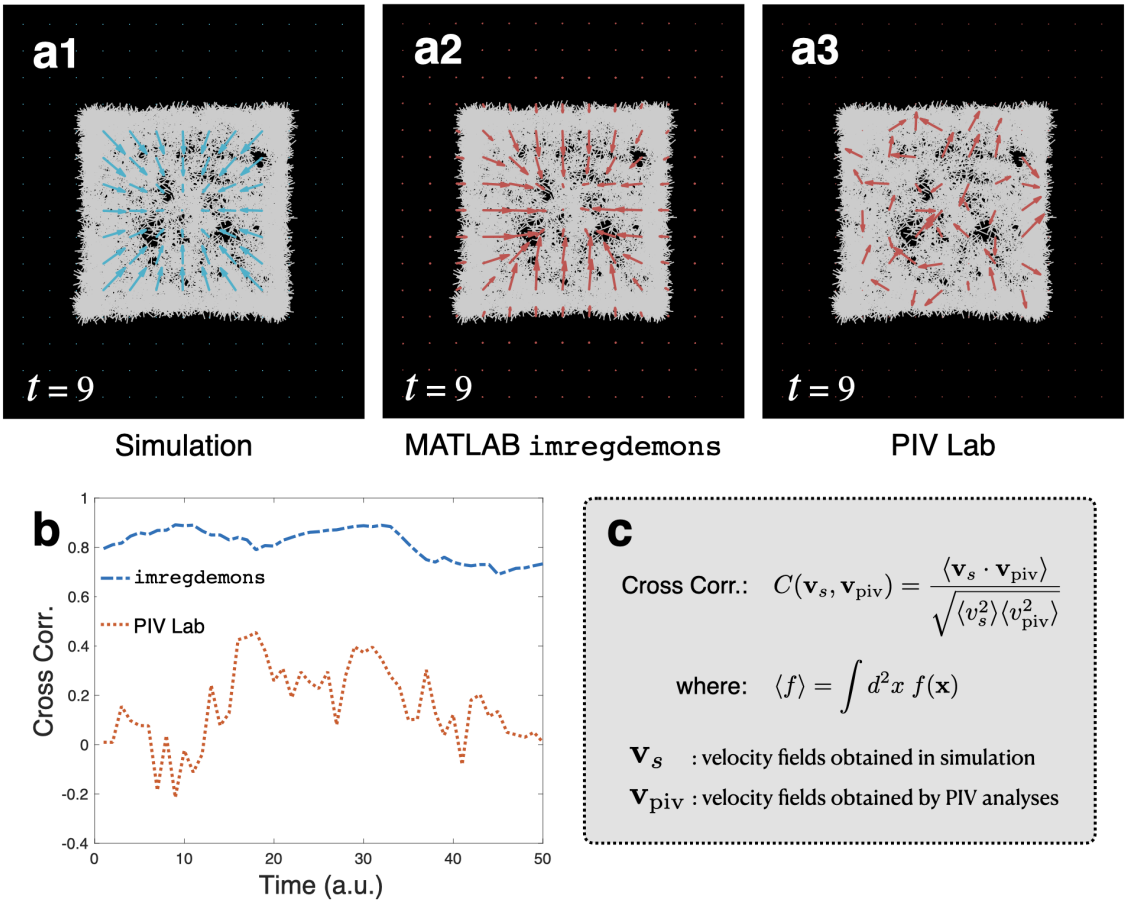

Supplementary Figure 1: **Validation and comparison of PIV analysis.** Top panels (a1,a2,a3) illustrate (for a single time point) the ground truth velocity field from numerical simulation (a1), and the predictions of the velocity fields using the imregdemons function of Matlab (a2) and PIVlab (a3). Panel (b) shows the cross-correlations between the $\mathbf{v}_{\rm s}$, and two PIV methods over the course of the network's contraction. The cross-correlation (defined in panel c) is normalized, hence bounded between $[-1, +1]$.

the original images by a factor of $\frac{1}{4}$ to make computation faster. Then we proceeded to correct the unevenness in illumination by computing a Gaussian blur and subtracting the resulting filter from every frame. Finally, we further reduced the noise by filtering the images using a scipy median filter [6].

To segment the microtubule networks from the background we applied the skimage implementation of two unsupervised thresholding algorithms, which are the Otsu and the triangle algorithms [8, 9]. The resulting microtubule network binary masks were assessed qualitatively, and we performed a series of binary morphological operations (erosion, dilation, opening, and closing), to remove unwanted small objects and to fill holes inside the area of the microtubule network.

To quantify the area corresponding to either microtubule network or plume, we up-scaled all masks to match the original raw image size. After that, we used numpy [10] to count all non-zero pixels in each mask and multiply the resulting count by the interpixel distance squared $(0.586\,\mu\text{m})^2$.

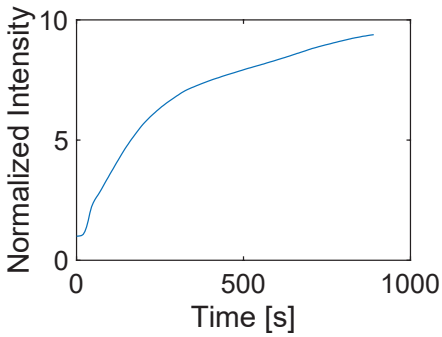

Supplementary Figure 2: **Normalized intensity within the illumination region increases over time.** The intensity, a summation of all pixel values within the illumination region, of the 600 µm square experiment is normalized by the one measured at the first frame of the experiment and plotted over time. It is seen that the normalized intensity increases, indicating an accumulation of microtubule filaments as a result of fluid flow mass transportation.

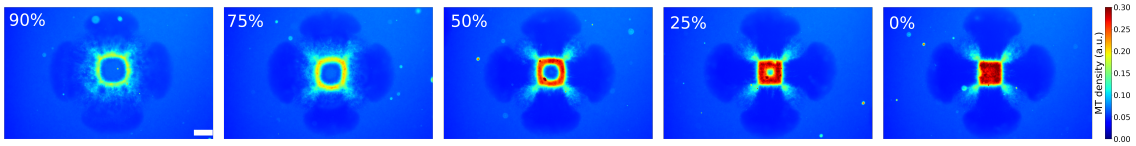

Supplementary Figure 3: **Microtubule density for the (hollow) square activation areas.** Here, the microtubule density is shown on a common color scale 130 s after the experiment started for cavity sizes of size 90%, 75%, 50%, 25%, and 0% (i.e., no hole) respectively. The scale bar is 100 µm. From the data it is clear, that when more of the system is activated, the more microtubules cluster in the center. However, in the corner region, no significant difference between the different experiments can be observed.

Supplementary Note 2: Additional experimental data for hollow square activation areas

In this section we include additional data on the microtubule density and flow fields for the hollow square networks. The figure Supplementary Figure 3 shows microtubule density as extracted by image analysis for hollow square networks. The hollow square networks consistently generate microtubule flux at the network corner during contraction. The internal density of the microtubule varies as a function of cavity size.

Supplementary Figure 4 provides images and flow fields for the 75% and 50% hollow networks to accompany Figure 2. The figure illustrates the experimental illumination pattern as well as the measured flow field as shown in Figure 2 for the 90% and 25% hollow networks.

Supplementary Note 3: Experimental flow field for circular activation area

In Supplementary Figure 5 we provide images and flow field measurements for a microtubule network induced by a 400 µm circular illumination pattern. The light pattern induces formation of a microtubule network and network contraction. However, the contracting network does not generate appreciable fluid flow. Supplementary Figure 5B provides quantification of the induced fluid flow field as measured by PTV and the corresponding vorticity. The measured flow field is negligible

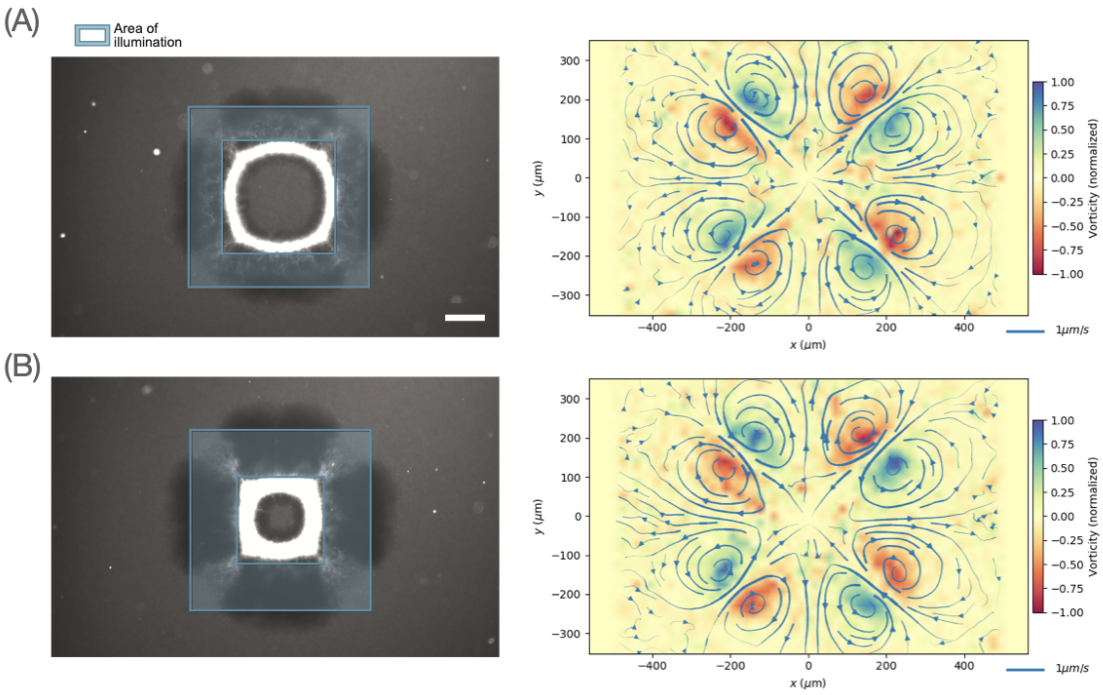

Supplementary Figure 4: **Additional flow fields for hollow activation areas.** The scale bar is 100 µm. The data here shows the same fluid flow behavior compared to the other hollow square areas shown in Figure 2, further demonstrating that the fluid flow for square illumination is independent of any cavities at the center.

with a median fluid velocity of $9.6\,\mathrm{nm\,s^{-1}}$ within the field of view. In Supplementary Figure 5C we compare the fluid velocity distribution for the circular illumination pattern to the distribution induced by other networks analyzed in the paper. The figure provides violin plots of the fluid speed distribution measured for each indicated network demonstrating that the circular network induces negligible fluid flow. In the violin plots whiskers indicate the minimum, median, and maximum of the measured fluid speed distribution.

Supplementary Methods 6: Theoretical Model and the corresponding Finite-Element Simulation

Due to the small length scales involved, the Reynolds number is small, so that the system can be described by the Stokes equation. For the sake of completeness, the Stokes equation in Eq. (1) is repeated here:

$$\mu\nabla^2\mathbf{v} - \nabla p + \mathbf{f} = 0, \qquad \nabla\cdot\mathbf{v} = 0, \tag{1}$$

where μ is the fluid viscosity, $\mathbf{v}$ is the fluid velocity, and p is the pressure. In the following, several geometric objects will be formally introduced, however, a visual representation of the geometry is presented in Supplementary Figure 6 to clarify the following description. The corner force hypothesis introduced in the main text is formally written as

$$\mathbf{f}(\mathbf{x}) \equiv \sum_i f_0\delta[\mathbf{x} - (x_i, y_i)]\,(-x_i, -y_i), \tag{2}$$

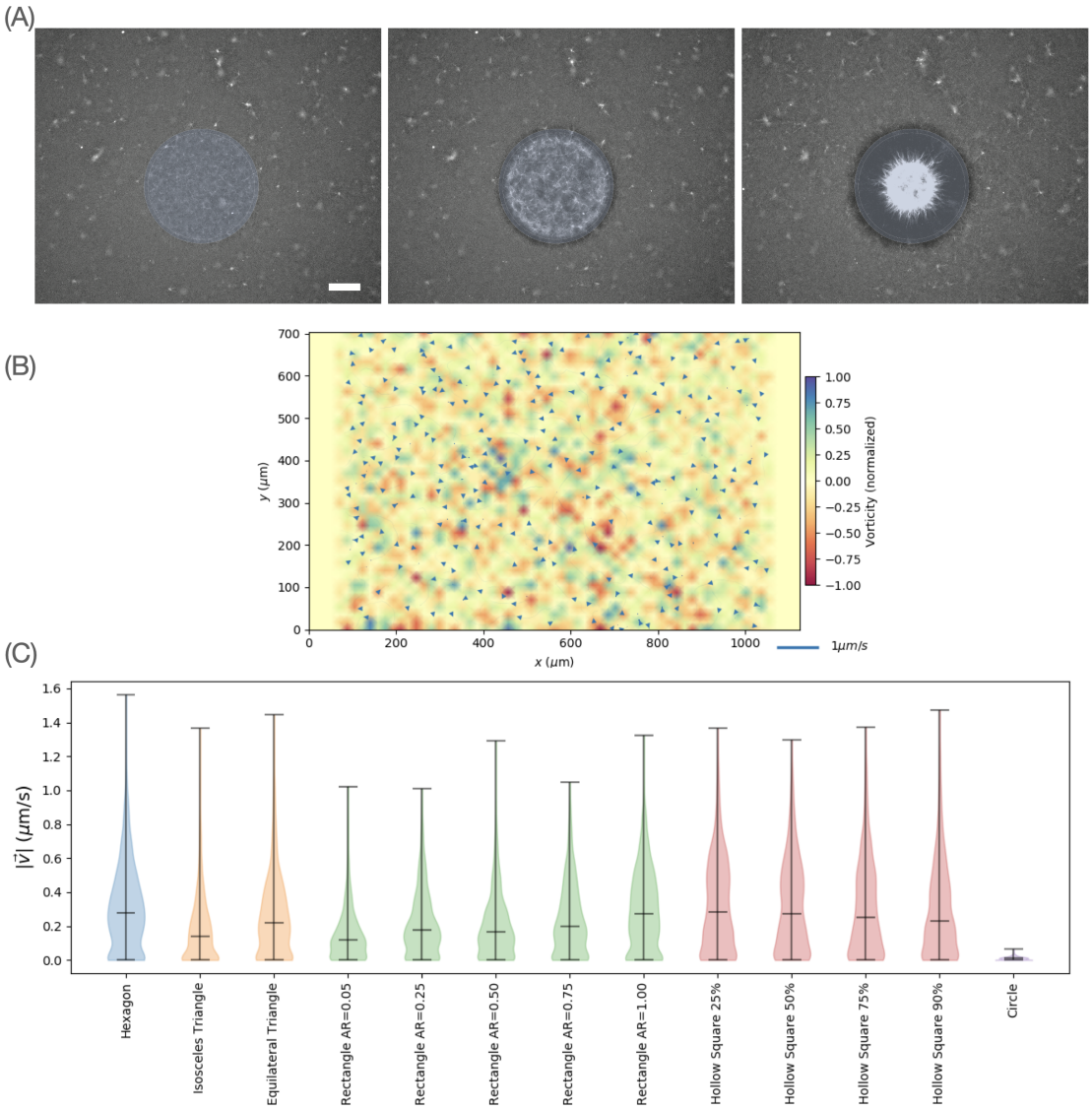

Supplementary Figure 5: **Circular illumination area generates minimal flow field.** (A) Images of microtubule density for circular activation area at times 10 s, 40 s, and 120 s after the beginning of the experiment, from left to right, respectively. Activation area is indicated as blue shading and scale bar is 100 µm (B) Flow field (arrows) and vorticity (color-scale) for the flow field generated by the microtubule network shown in (A), where it can be observed that no organized fluid flow emerges. (C) Violin plot of fluid speed distribution for flow fields analyzed in the paper. Each violin plot displays the distribution of fluid speeds within the experimental field of view for a given illumination geometry. Whiskers indicate minimum, maximum, and median of the fluid speed measurements. This plot shows that the circular illumination region generates a flow field with min, max, and median that are substantially lower than polygonal light patterns. The median flow generated by the circular illumination within the experimental field of view is 9.6 nm s^{-1}.

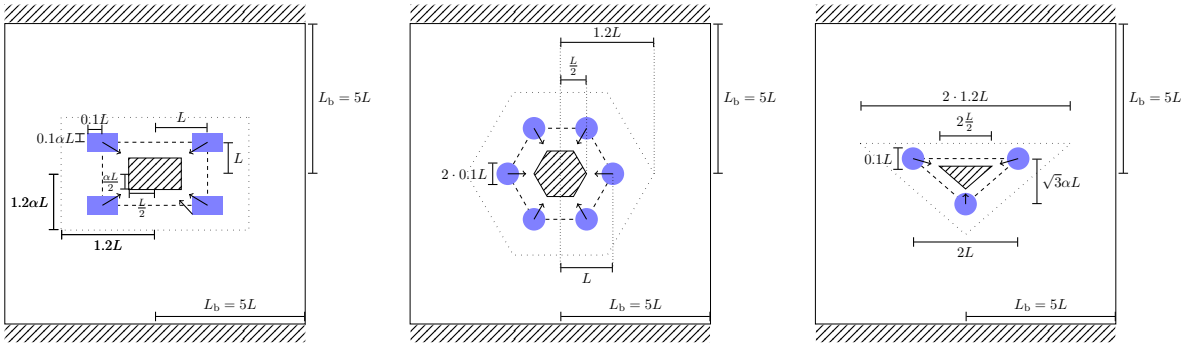

(a) Rectangle (b) Hexagon (c) Triangle

Supplementary Figure 6: **Overview figure of the different geometries used in the simulation.** It should be noted that the figures are not to scale. In these figures, the shaded regions denote areas with no-slip boundaries, and the blue regions mark regions with non-vanishing force density. The outer solid line demarcates the simulation cell, where the left and right boundary have open boundary conditions. The dashed line marks the activation area (compared to the experiment, with no influence on the simulation) and the dotted line indicates the change in meshing from a fine mesh in the center to a coarser mesh outside. For the rectangle and the triangle, α denotes the aspect ratio so that $\alpha = 1$ denotes the square and equilateral triangle, respectively.

where i enumerates the corners of the activated polygon. The points (x_i, y_i) describe the coordinates of the corners, so that the delta-function encodes the point-force condition. Using a coordinate system which places the center of mass at the origin of the simulation, the vector $(-x_i, -y_i)$ describes that the forces points towards the center of the structure. For example, if the rectangle with aspect ratio α is simulated, then the origin in the simulation is at the center of the rectangle, and the four corners are located at $(\pm L, \pm \alpha L)$.

Additional to the Stokes equation describing the bulk, boundary conditions are required to completely define the problem. As described in the main text, there are two sets of boundary conditions, the first describing a no-slip boundary at the central jamming region. In particular it was assumed that $\mathbf{v}(\mathbf{x}) \equiv 0$ for all $\mathbf{x}$ in the central region with half the linear dimension. For example for the rectangle with aspect ratio α, the velocity is forced to vanish in the inner rectangle spanned by the four points $(\pm L/2, \pm \alpha L/2)$. The second set of boundary conditions is enforced along the boundaries of the short axis of the fluid cell. We chose a simulation domain, so that the boundaries along the short axis coincide with the physical boundaries. Hence, the second set of no-slip boundary conditions is $\mathbf{v}[(x, y)] \equiv 0$ if $y = \pm L_\mathrm{b}$, where L_b is the size of the simulation box. It should be noted that there were no additional boundary conditions implemented for the long axis, since in the experiment these boundaries are sufficiently far away from the light-activated area, so that no boundary effect should be expected.

In our particular case, non-dimensionalized values were used with $\mu = f_0 = L = 1$. Therefore, the simulation cell size in non-dimensionalized form is $L_\mathrm{b} = 3\,\mathrm{mm}/600\,\mu\mathrm{m} \times L = 5L$. Since FEM simulations cannot handle point-forces consistently, the point force was spread out over a small region in the corners. In particular, for the rectangular case, the delta-function in Equation (2) was replaced with

$$\delta[(x, y) - (x_i, y_i)] \mapsto \chi \left[\left(|x - x_i| < \frac{L}{10} \right) \wedge \left(|y - y_i| < \frac{\alpha L}{10} \right) \right], \tag{3}$$

where χ is the indicator function, being 1 where the argument is true, and being 0 otherwise. This describes small rectangles in the corners describing the non-vanishing forces. For the hexagonal and

triangular cases, rather than repeating the same structure, small circles with radius $r = \frac{L}{10}$ were chosen. Formally, this equates to the replacement

$$\delta[(x, y) - (x_i, y_i)] \mapsto \chi \left[\|\mathbf{x} - (x_i, y_i)\| < \frac{L}{10} \right]. \tag{4}$$

The meshing contained initially 60×60 equal-distance points, and in a central region of $1.2 \times L$ the meshing was refined twice, increasing the local meshing density by a factor of 4. The Stokes equation was then solved with Taylor-Hoods finite-elements.

Our implementation of this code can be found on GitHub: `https://github.com/domischi/StokesFEM`, which is based on the FeniCS library [11].

Supplementary Note 4: Theoretical description of circular activation area

The theoretical model presented in the manuscript is based on corners, and hence does not describe the circle. However, the circle can be understood as the limiting shape of a regular N-gon for large N. We analyze this limiting process by finding the flow field for regular N-gons, putting a point force in each of the corners in analogy to the main manuscript. It should be noted that, due to limitations of the FEM code, we only consider a Stokeslet solution which ignores the boundary conditions. In two dimensions, the Stokeslet solution for the fluid velocity at position $\mathbf{x}$ is

$$\mathbf{u}(\mathbf{x}) = -\log(|\mathbf{x}|)\mathbf{f} + \frac{\mathbf{f} \cdot \mathbf{x}}{|\mathbf{x}|^2}\mathbf{x}, \tag{5}$$

for a point force $\mathbf{f}$ at the origin [12].

The results for the radial velocity (Supplementary Figure 7) demonstrate that the larger N, i.e., the more the N-gon resembles a circle, the smaller becomes the region with non-vanishing fluid flow. This prediction of vanishing fluid flow is in good agreement with the experiment, demonstrating that our model can be extended to the circular case almost everywhere (except for points along the circle circumference).

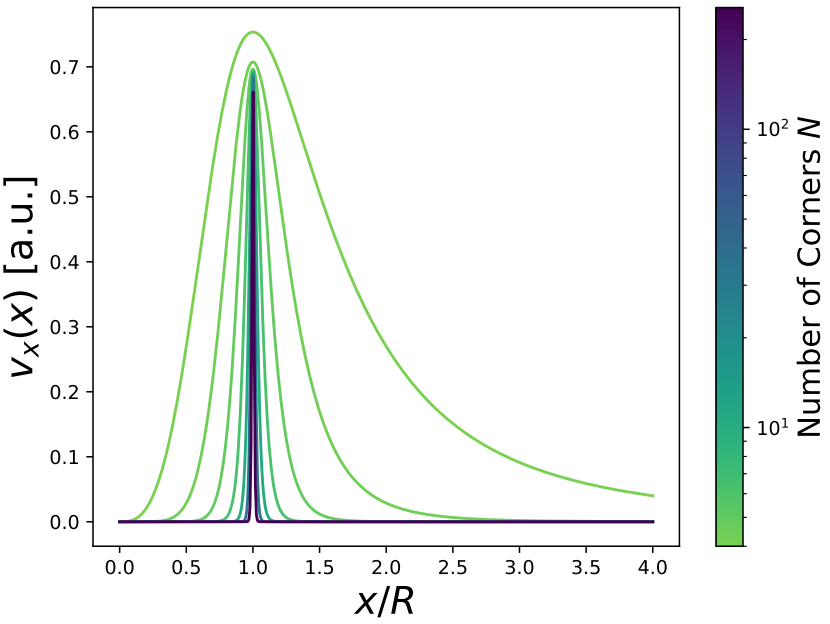

Supplementary Figure 7: **Radial velocity for regular N-gons as a function of distance.** It can be observed that for more circle like shapes (larger N, darker colors), the region of non-vanishing velocities becomes smaller, localized along $x = R$, where R is the radius of the circumscribed circle. Because this is in good agreement with the experiment, it demonstrates that our model is extendable to the case of circular activation areas everywhere except $x = R$.

Supplementary Movies

Bright field videos are provided for eight illumination patterns. In each movie, image frames are acquired every five seconds. The time stamp is given in minutes:seconds and a 100 µm scale bar is indicated. The movie shows dynamics of the 1 µm tracer beads used to quantify fluid flow and the microtubule network is also visible.

Supplementary Movie 1

Video of 600 µm square network from Figure 1.

Supplementary Movies 2

Video of 400 µm rectangular network with aspect ratios of .75 from Figure 3.

Supplementary Movies 3

Video of 400 µm rectangular network with aspect ratios of .5 from Figure 3.

Supplementary Movies 4

Video of 400 µm rectangular network with aspect ratios of .25 from Figure 3.

Supplementary Movies 5

Video of 400 µm rectangular network with aspect ratios of .05 from Figure 3.

Supplementary Movies 6

Video of hexagon networks from Figure 4.

Supplementary Movies 7

Video of equal angle triangle from Figure 4.

Supplementary Movies 8

Video of isosceles triangle from Figure 4.

Supplementary References

[1] Lau, A., Prasad, A., and Dogic, Z., "Condensation of isolated semi-flexible filaments driven by depletion interactions," *EPL (Europhysics Letters)*, Vol. 87, No. 4, 2009, pp. 48006.

[2] Ross, T. D., Lee, H. J., Qu, Z., Banks, R. A., Phillips, R., and Thomson, M., "Controlling organization and forces in active matter through optically defined boundaries," *Nature*, Vol. 572, No. 7768, 2019, pp. 224–229.

[3] Adamczyk, A. and Rimai, L., "2-Dimensional particle tracking velocimetry (PTV): technique and image processing algorithms," *Experiments in fluids*, Vol. 6, No. 6, 1988, pp. 373–380.

[4] Schmidt, T., Schütz, G., Baumgartner, W., Gruber, H., and Schindler, H., "Imaging of single molecule diffusion," *Proceedings of the National Academy of Sciences*, Vol. 93, No. 7, 1996, pp. 2926–2929.

[5] MATLAB, *version 9.6 (R2019a)*, The MathWorks Inc., Natick, Massachusetts, 2019.

[6] Virtanen, P., Gommers, R., Oliphant, T. E., Haberland, M., Reddy, T., Cournapeau, D., Burovski, E., Peterson, P., Weckesser, W., Bright, J., van der Walt, S. J., Brett, M., Wilson, J., Jarrod Millman, K., Mayorov, N., Nelson, A. R. J., Jones, E., Kern, R., Larson, E., Carey, C., Polat, İ., Feng, Y., Moore, E. W., Vand erPlas, J., Laxalde, D., Perktold, J., Cimrman, R., Henriksen, I., Quintero, E. A., Harris, C. R., Archibald, A. M., Ribeiro, A. H., Pedregosa, F., van Mulbregt, P., and Contributors, S. . ., "SciPy 1.0: Fundamental Algorithms for Scientific Computing in Python," *Nature Methods*, Vol. 17, 2020, pp. 261–272.

[7] Van der Walt, S., Schönberger, J. L., Nunez-Iglesias, J., Boulogne, F., Warner, J. D., Yager, N., Gouillart, E., and Yu, T., "scikit-image: image processing in Python," *PeerJ*, Vol. 2, 2014, pp. e453.

[8] Otsu, N., "A threshold selection method from gray-level histograms," *IEEE transactions on systems, man, and cybernetics*, Vol. 9, No. 1, 1979, pp. 62–66.

[9] Zack, G. W., Rogers, W. E., and Latt, S. A., "Automatic measurement of sister chromatid exchange frequency." *Journal of Histochemistry & Cytochemistry*, Vol. 25, No. 7, 1977, pp. 741–753.

[10] Harris, C. R., Millman, K. J., van der Walt, S. J., Gommers, R., Virtanen, P., Cournapeau, D., Wieser, E., Taylor, J., Berg, S., Smith, N. J., et al., "Array programming with NumPy," *Nature*, Vol. 585, No. 7825, 2020, pp. 357–362.

[11] Alnæs, M. S., Blechta, J., Hake, J., Johansson, A., Kehlet, B., Logg, A., Richardson, C., Ring, J., Rognes, M. E., and Wells, G. N., "The FEniCS Project Version 1.5," *Archive of Numerical Software*, Vol. 3, No. 100, 2015.

[12] Chwang, A. T. and Wu, T. Y. T., "Hydromechanics of low-Reynolds-number flow. Part 2. Singularity method for Stokes flows," *Journal of Fluid Mechanics*, Vol. 67, No. 4, 1975, pp. 787–815.